Effect of tert-Butyl Functionalization on the Photoexcited Decay of a Fe(II)-N-Heterocyclic Carbene Complex

Pápai, Mátyás Imre; Penfold, Thomas J.; Møller, Klaus Braagaard

Published in:
The Journal of Physical Chemistry Part C

Link to article, DOI:
10.1021/acs.jpcc.6b05023

Publication date:
2016

Document Version
Peer reviewed version

The Effect of *tert*-Butyl Functionalization on the Photoexcited Decay of a Fe(II)-*N*-Heterocyclic Carbene Complex

Mátyás Pápai,[*,†,‡] Thomas J. Penfold,[¶] and Klaus B. Møller[†]

†*Department of Chemistry, Technical University of Denmark, DK-2800, Kongens Lyngby, Denmark*

‡*Wigner Research Centre for Physics, Hungarian Academy of Sciences, 'Lendület' (Momentum) Spectroscopy Research Group, P.O. Box 49, H-1525 Budapest, Hungary*

¶*School of Chemistry, Newcastle University, Newcastle upon Tyne, NE1 7RU, United Kingdom*

E-mail: papai@kemi.dtu.dk

Phone: +45-21378822

Abstract

Understanding, and subsequently, being able to manipulate the excited state decay pathways of functional transition metal complexes, is of utmost importance in order to solve grand challenges in solar energy conversion and data storage. Herein we perform quantum chemical calculations and spin-vibronic quantum dynamics simulations on the Fe-*N*-heterocyclic carbene (NHC) complex, $[Fe(btbip)_2]^{2+}$ (btbip = 2,6-bis(3-*tert*-butyl-imidazole-1-ylidene)pyridine). The results demonstrate that a relatively minor structural change compared to its parent complex, $[Fe(bmip)_2]^{2+}$ (bmip = 2,6-bis(3-methyl-imidazole-1-ylidene)-pyridine), completely alters the excited state relaxation. Ultrafast deactivation of the initially excited metal-to-ligand charge transfer (^{1,3}MLCT) states occur within 350 fs. In contrast to the widely adopted mechanism of Fe(II) photophysics, these states decay into close-lying singlet metal-centered (^{1}MC) states. This occurs because the *tert*-butyl functionalization stabilizes the ^{1}MC states, enabling the ^{1,3}MLCT $\rightarrow$ ^{1}MC population transfer to occur close to the Franck-Condon geometry, making the conversion very efficient. Subsequently, a spin cascade occurs within the MC manifold leading to the population of triplet and quintet MC states. These results will inspire highly-involved ultrafast experiments performed at X-ray Free Electron Lasers (XFELs) and shall pave the way for the design of novel high efficiency transition metal-based functional molecules.

Introduction

Controlling the properties of versatile transition metal complexes is of great interest for developing a broad range of new efficient technologies. A significant amount of the research effort in this area has been dedicated to earth-abundant Fe(II) complexes, with particular focus on the spin crossover (SCO) phenomenon.[1] In SCO, the magnetic properties of the complex may be manipulated using an external perturbation which flips the spin state between a low-spin (LS) ground state and a high-spin (HS) metastable excited state. When this transition is initiated by light, the process is known as the light-induced excited spin state

trapping (LIESST),[2,3] which has been intensely studied owing to its rich ultrafast excited state decay dynamics.

A model complex for the LIESST mechanism is the Fe(II) polypyridine complex, $[Fe(bipy)_3]^{2+}$ (bipy = 2,2'-bipyridine), which exhibits an ultrafast excited state decay from the photoactive metal-to-ligand charge transfer (MLCT) to low-lying metal-centered (MC) states in ∼150 fs.[4–7] These dynamics have stirred significant interest, not just in an academic setting, but also with potential applications of spin trapping in optical writing/magnetic reading for high data density storage devices.[8–10] Fe(II) polypyridine complexes were also considered as potential candidates for cheap and Earth-abundant dye-sensitized solar cells (DSSCs).[11] But it was soon realized that the low-lying MC states transfer the photoexcited electrons away from outer ligand-based regions of the complex, preventing charge transfer and/or injection making them unsuitable for such devices.[12]

However, Liu *et al.* have recently demonstrated that this puzzle can be solved by exploiting the strong field effects of *N*-heterocyclic carbene (NHC) ligands.[13,14] Indeed, the authors found that in $[Fe(bmip)_2]^{2+}$ (bmip=2,6-bis(3-methyl-imidazole-1-ylidene)pyridine), the ultrafast intersystem crossing (ISC) between the photoexcited ^{1}MLCT state and the ^{3}MLCT state is followed by a relatively slow 9 ps ^{3}MLCT decay (Figure 1 right). This ^{3}MLCT lifetime is two-three order of magnitude longer compared to those of other known Fe molecular compounds. Proceeding this, Harlang *et al.* showed that a carboxylic acid derivative of $[Fe(bmip)_2]^{2+}$ can be used as a photosensitizer on the surface of TiO_2 resulting in ∼92% electron injection from the photoexcited complex to the semiconductor nanoparticle.[15] This demonstrates that the critical electron injection step, necessary for technologies such as DSSCs,[16] photocatalysts for water splitting[17,18] and CO_2 reduction,[19] can be achieved using Earth-abundant transition metal complexes. Unfortunately, >85% of the injected electrons at the $[Fe(bmip)_2]^{2+}$-TiO_2 interface undergo fast (<10 ns) electron-cation recombination. This severely restricts the potential functional performance of this material, and therefore calls for continued development aimed to prolong MLCT lifetimes or strategies for slowing

down electron recombination.

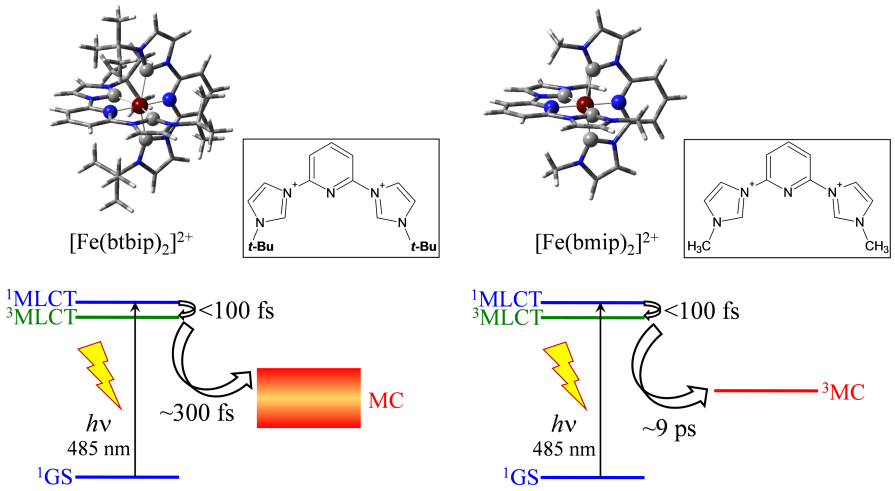

Figure 1: Illustration of the molecular structure and photophysics of $[Fe(btbip)_2]^{2+}$ (left) and $[Fe(bmip)_2]^{2+}$ (right). Chemical structures of the free btbip and bmip ligands are also shown. Characteristic relaxation lifetimes are taken from ref. 13.

The structural modification of the NHC ligands, which is the subject of the present work, is challenging due to the high density of low-lying excited electronic states of Fe(II) complexes, meaning that many potential photoexcited decay pathways exist. The first functionalization of $[Fe(bmip)_2]^{2+}$ was reported by Liu *et al.* and involved the 3-*tert*-butyl (*t*-Bu) substitution on the carbene ligands leading to the creation of $[Fe(btbip)_2]^{2+}$ (btbip = 2,6-bis(3-*tert*-butyl-imidazole-1-ylidene)pyridine).[13] Strikingly, this latter Fe(II)-NHC complex was found to exhibit completely different photophysics from $[Fe(bmip)_2]^{2+}$. More like the excited state dynamics of $[Fe(bipy)_3]^{2+}$,[4–7] the MLCT lifetime of this complex was found to be 300 fs, as determined by transient optical absorption spectroscopy (Figure 1 left).[13] Crucially, these rather profound ligand-dependent photophysical variations strongly motivate a detailed understanding of the excited state dynamics of Fe(II)-NHC complexes, which could potentially lead to design rules aimed to control photorelaxation processes.

To achieve this mechanistic understanding, theory and computations play an important role along side time-resolved experiments. One of the first computational attempts to reveal the details of the excited state dynamics of the discussed complexes was a quantum chemical

study of the excited state potential energy surfaces of $[Fe(bmip)_2]^{2+}$ by Fredin *et al.*[20] This work confirmed that the application of strongly σ-donating bmip ligands led to the destabilization of MC states, with only the three components of the $^3T_1$ MC state below the lowest MLCTs. These authors also proposed that the origin of the increased ^{3}MLCT lifetime was due to the shallow nature of its potential. This work was recently extended by Pápai *et al.*, who studied the spin-vibronic dynamics,[21] utilizing a similar approach to the one used previously for first[22] and third-row[23–25] transition metal complexes. This study revealed that the reason for the increased ^{3}MLCT lifetime of $[Fe(bmip)_2]^{2+}$ is that the population transfer to the ^{3}MC states occurs in a region of the potential energy surface, where the energy gap between the ^{3}MLCT and ^{3}MC states is large, making the conversion inefficient. Herein we use quantum chemical calculations and wavepacket quantum dynamics simulations to study the effect of *tert*-butyl functionalization of $[Fe(bmip)_2]^{2+}$ on the MLCT photodynamics. Importantly, we show a deactivation mechanism proceeding via a ^{1,3}MLCT$\rightarrow{}^1$MC relaxation channel. The ^{1}MC, usually neglected in the decay of photoexcited molecules, is demonstrated to be crucial in the investigated *tert*-butyl-substituted carbene complex. These simulations demonstrate how the excited state relaxation of these Fe(II)-NHC complexes can be controlled by relatively minor changes in the ligand sphere paving the way for the computational design of high-efficiency transition metal-based functional molecules.

Theory and Computational Methods

Spin-Vibronic Hamiltonian and Quantum Chemical Calculations

The model Hamiltonian applied in the present work is based upon the vibronic coupling Hamiltonian (VCHAM),[26,27] which has been widely used to simulate excited state nonadiabatic dynamics on a wide variety of systems.[28–33] This approach is often the method of choice for quantum dynamics, when photophysical processes are studied and therefore no large amplitude nuclear motion exist. This is because of the requirement to use the dia-

batic electronic basis to avoid the divergence of couplings which exist within the adiabatic representation. It also exploits the fact that while transformation from the adiabatic to the diabatic representation is normally difficult to perform, the opposite way (i.e., diabatic to adiabatic) is relatively simple using a unitary transformation. Consequently, starting from an initial guess, the diabatic potential can be refined using least squares fit to the adiabatic potential computed using quantum chemical methods. At each iteration of the fit, the diabatic Hamiltonian is transformed into the adiabatic basis to assess the quality of the fit. This method is often referred to as *diabatization by ansatz*.

The vibronic coupling Hamiltonian is obtained by performing a low-order, usually linear or second-order, Taylor expansion around the $\mathbf{Q}_0$ reference point, where the diabatic and adiabatic bases are defined to be identical, in the present case, the Franck-Condon (FC) geometry:

$$\mathbf{H} = \mathbf{H}^{(0)} + \mathbf{W}^{(0)} + \mathbf{W}^{(1)} + \mathbf{W}^{(2)} + ... \tag{1}$$

The zeroth-order Hamiltonian ($\mathbf{H}^{(0)}$) is composed of the kinetic and potential energy operators of the ground state harmonic oscillator characterized by the ω_n vibrational frequencies and Q_n dimensionless (mass-frequency scaled) normal coordinates. In the case of a model system possessing i electronic states, the $i \times i$ $\mathbf{W}^{(0)}$, $\mathbf{W}^{(1)}$, and $\mathbf{W}^{(2)}$ matrices describe the zeroth, first, and second-order potential-like coupling terms. The zeroth-order matrix is diagonal and contains the energy of each excited state at $\mathbf{Q}_0$. The first-order coupling matrices are expressed as:

$$W_{ij}^{(1)} = \sum_n \left\langle \Phi_i(\mathbf{Q}_0) \left| \frac{\partial \hat{H}_{el}}{\partial Q_n} \right| \Phi_j(\mathbf{Q}_0) \right\rangle Q_n \tag{2}$$

where the on-diagonal and off-diagonal terms are written:

$$W_{ii}^{(1)} = \sum_n \kappa_n^{(i)} Q_n \tag{3a}$$

$$W_{ij}^{(1)} = \sum_n \lambda_n^{(i,j)} Q_n \tag{3b}$$

Here $\hat{H}_{\mathrm{el}}$ is the electronic (clamped nucleus) Hamiltonian, and Φ_i,Φ_j are the diabatic electronic wavefunctions, respectively. $\kappa_n^{(i)}$ and $\lambda_n^{(i,j)}$ are the expansion coefficients corresponding to the on- and off- diagonal matrix elements, respectively. The former are the forces acting within an electronic surface and are responsible for structural changes of excited state potentials compared to the one of the ground state. The latter accounts for the nonadiabatic coupling between different excited states. Second order terms are included in a similar manner and are written as:

$$W_{ij}^{(2)} = \frac{1}{2}\sum_{n,m}\left\langle \Phi_i(\mathbf{Q}_0)\left|\frac{\partial^2 \hat{H}_{el}}{\partial Q_n Q_m}\right|\Phi_j(\mathbf{Q}_0)\right\rangle Q_n Q_m \tag{4}$$

Only the on-diagonal quadratic coupling constants (i.e., $Q_n = Q_m$, referred to as $\gamma_n^{(i)}$) are used in the present study.

Since $[\mathrm{Fe(btbip)_2}]^{2+}$ has 291 nuclear degrees of freedom (DOF), the full dynamical treatment of the unconstrained nuclear configuration space within a wavepacket propagation approach is unrealistic. To overcome this, we have constructed a 4-dimensional model Hamiltonian designed to capture the core physical processes during the excited state dynamics of $[\mathrm{Fe(btbip)_2}]^{2+}$. This is achieved by firstly calculating the ground state normal modes of the complex at the B3LYP*[34]/TZVP level of theory utilizing $\mathrm{D_{2d}}$ point group symmetry. All frequencies were found to be positive, confirming that the geometry corresponding to the FC point is a true minimum of the potential energy surface (PES). Subsequently, we have selected the 4 most important vibrational modes for the dynamics by i) identifying the most significant structural distortions at minimum energy geometries of excited states (this yielded the selection of low-frequency Fe-N/Fe-C stretching modes), ii) utilizing the magnitude of linear vibronic coupling constants ($\kappa_n^{(i)}$ and $\lambda_n^{(i,j)}$), and iii) using point group symmetry to determine the modes for which important linear coupling elements could be non-zero. It is noted that the use of symmetry is not essential, but it significantly simplifies the problem as many of the couplings are identified to be zero. Without symmetry, accurate quantum

dynamics are still potential, but the development of the Hamiltonian is a little more complex as recently demonstrated by Harabuchi *et al.*[25]

In the present model Hamiltonian, all electronic states with an excitation energy at the FC geometry below those of the initially excited S_4,S_5 ^{1}MLCT states were included. The application of this criteria led to 5 singlet and 10 triplet spin-free states. Potential energy curves of these states were calculated by performing TD-DFT computations at the FC point and geometries displaced along the 4 normal modes. These computations were carried out with the application of the TD-B3LYP*/TZVP method utilizing the Tamm-Dancoff (TDA) approximation[35] as implemented in the ORCA3.0 quantum chemistry program package.[36] It is important to point out that the TD-B3LYP* method was proven to correctly reproduce the PESs of Fe(II) complexes, computed at the higher, multiconfigurational second-order perturbation theory (CASPT2) level of theory.[5,37–39] Moreover, typical qualitative failures of TD-DFT describing the topology of PESs, e.g., conical intersections, due to the involvement of a closed-shell ground state in the crossing with an open-shell excited state and/or the presence of significant double excitation character,[40] are avoided. This is because, in the present study, we consider dynamics only between open-shell excited states, which can be generated by a single excitation from the ground state.

The diabatic potentials were extracted from the above calculations by analyzing the composition of the obtained excitations and the atomic contributions of the involved Kohn-Sham orbitals. In Figures S3–S7, we illustrate the MC or MLCT character of the considered singlet excited states by presenting their donor and acceptor natural transition orbitals (NTOs)[41] obtained at the FC geometry. The occupation numbers corresponding to these NTOs were all found to be above 0.90. The adiabatically ordered TD-DFT energies along the normal modes were then fitted with the second-order vibronic coupling model described above using harmonic potentials. The fit was performed separately for singlet and triplet spin-free potential energy curves leading to the $\kappa_n^{(i)}$, $\lambda_n^{(i,j)}$, and $\gamma_n^{(i)}$ values given in Tables S3-S5 and the results shown in Figure 3. The coupling between the two manifolds to create the spin-

vibronic potentials was treated as a perturbation to the spin-free potential energy curves and was achieved by including the SOC matrix elements between all considered excited states computed at the B3LYP*/ZORA[42,43]/TZP level utilizing the perturbative method[44] of T. Ziegler *et al.* as implemented in the ADF2014.07 code.[45] This resulted in the spin-vibronic Hamiltonian used in the quantum dynamics simulations.

Quantum Dynamics Simulations

The wavepacket quantum dynamics simulations were performed using the multiconfiguration time-dependent Hartree (MCTDH) method as implemented in the Heidelberg MCTDH program package.[46,47] This method offers an efficient algorithm for solving the time-dependent Schrödinger equation utilizing a multiconfigurational series of Hartree products of single particle functions (SPFs) as *ansatz*:

$$\Psi(Q_1,...,Q_f,t) = \sum_{j_1=1}^{n_1} ... \sum_{j_f=1}^{n_f} A_{j_1...j_f}(t)\varphi_{j_1}^{(1)}(Q_1,t)...\varphi_{j_f}^{(f)}(Q_f,t) \tag{5}$$

where $A_{j_1...j_f}(t)$ and $\varphi_{j_1}^{(1)}(Q_1,t)...\varphi_{j_f}^{(f)}(Q_f,t)$ are the sets of variatonally optimized time-dependent expansion coefficients and basis functions, i.e., SPFs, respectively, for f number of nuclear DOF. The SPFs are then further expanded in a time-independent primitive basis set, in the present case, into harmonic oscillator (HO) basis functions (χ_k^i):

$$\varphi_j^n = \sum_{k=1}^{N_n} a_{kj}^{(n)} \chi_k^n(Q_n) \tag{6}$$

While, like standard grid based wavepacket propagation methods, the computational effort of this approach still suffers from exponential scaling, it benefits from the fact that i) the SPFs are variationally determined so less are required for convergence and ii) the functions can be multi-dimensional particles containing more than one DOF thus reducing their effective number.

The excited state quantum dynamics simulations using the 36 state, 4 mode spin-vibronic Hamiltonian were initiated by impulsive excitation of the ground state wavepacket, built using one-dimensional harmonic oscillator functions with zero initial momentum, into the lowest singlet MLCT states, i.e., S_4 and S_5. The computational details are shown in Table 1 and ensured converged dynamics for the full 2 ps of the excited state simulations. Note that in the below table n_i is only shown for those components of triplets states which were significantly populated in the dynamics. Due to molecular symmetry, the remaining triplets were very weakly populated, and for these, in order to reduce the computational cost, n_i was set to 5. Test computations showed that lowering n_i for these states did not have any considerable effect on the simulated dynamics.

Table 1: Computational details of the MCTDH simulations using the 36 state, 4 mode spin-vibronic Hamiltonian. N_n is the number of primitive harmonic oscillator basis functions used for each mode. n_i are the number of single particle functions used to describe the wavepacket in each state.

Modes	N_n	n_{S_0},n_{S_1},n_{S_2},n_{S_3},n_{S_4},n_{S_5},n_{T_1},n_{T_2},n_{T_3},n_{T_4},n_{T_5},n_{T_6},n_{T_7},n_{T_8},n_{T_9},$n_{T_{10}}$
ν_4	121	1,20,20,20,20,20,20,20,20,20,20,20,20,20,20,20
ν_{11}	61	1,20,20,20,20,20,20,20,20,20,20,20,20,20,20,20
ν_{16}	71	1,20,20,20,20,20,20,20,20,20,20,20,20,20,20,20
ν_{33}	71	1,20,20,20,20,20,20,20,20,20,20,20,20,20,20,20

Results and discussion

In the proceeding section, we present a quantum chemical exploration of excited state potential energy curves along the normal mode most prominent for driving the photodynamics of $[Fe(btbip)_2]^{2+}$, which provides a qualitative picture of its deactivation mechanism. Subsequently, we use the potentials computed along the 4 vibrational modes to develop a model spin-vibronic Hamiltonian and perform quantum dynamics simulations to reveal the details of the decay mechanism.

Excited-state deactivation via the Dominant Vibrational Mode

The photoexcited dynamics of Fe(II) complexes are usually cast in terms of one vibrational mode related to symmetric bond length changes in the first coordination sphere, i.e., a breathing mode. Figure 2 depicts the DFT/TD-DFT potential energy curves of the ground and excited electronic states relevant to the photodynamics, along the lowest-frequency breathing normal mode of $[Fe(btbip)_2]^{2+}$, ν_4, found to exhibit the most prominent changes relative to the ground state potential.

The calculated ^{1}MLCT-^{3}MLCT energetics are in good accordance with the initial steps of the mechanism summarized in Figure 1. First, the 2.5 eV excitation energy of the lowest optically bright S_4,S_5 ^{1}MLCT states at the FC geometry is in very good accordance with the lowest band of the absorption spectrum,[13] which was excited experimentally using a 485 nm laser. Furthermore, the (quasi-)degeneracy of the S_4,S_5 and T_{10} MLCT states is consistent with the <100 fs ultrafast ISC reported in ref. 13.

Notably, compared to the MC states of $[Fe(bmip)_2]^{2+}$,[20,21] all MC potentials of $[Fe(btbip)_2]^{2+}$ show a strong, ca. 0.5 eV stabilization. This is attributed to the ∼0.13 Å increase of the Fe-C bond distances caused by the steric repulsion of the bulky *tert*-butyl groups in $[Fe(btbip)_2]^{2+}$, favoring the antibonding character of MC states. Interestingly, among these stabilized MC states, the ^{1}MCs are lowered such that they intersect the MLCT states close to the FC geometry, opening the potential for very fast ^{1,3}MLCT deactivation, consistent with the dynamics reported by Liu *et al.*[13] Without the presence of these ^{1}MC states, the excited state potentials are rather reminiscent of those of $[Fe(bmip)_2]^{2+}$. This means that the deactivation of MLCT states, via the MC manifold, would have to occur by overcoming a large ca. 0.5 eV ^{3}MLCT-^{3}MC energy gap, which would likely lead to an extremely slow ^{3}MLCT decay. After conversion to the ^{1}MCs, the system is expected to undergo a relaxation cascade within the MC manifold, leading to population transfer to ^{3}MC, and subsequently to ^{5}MC states. These results suggest the ^{1}GS→^{1}MLCT→^{3}MLCT→^{1}MC→^{3}MC→^{5}MC deactivation pathway, as illustrated by the yellow arrows in Figure 2.

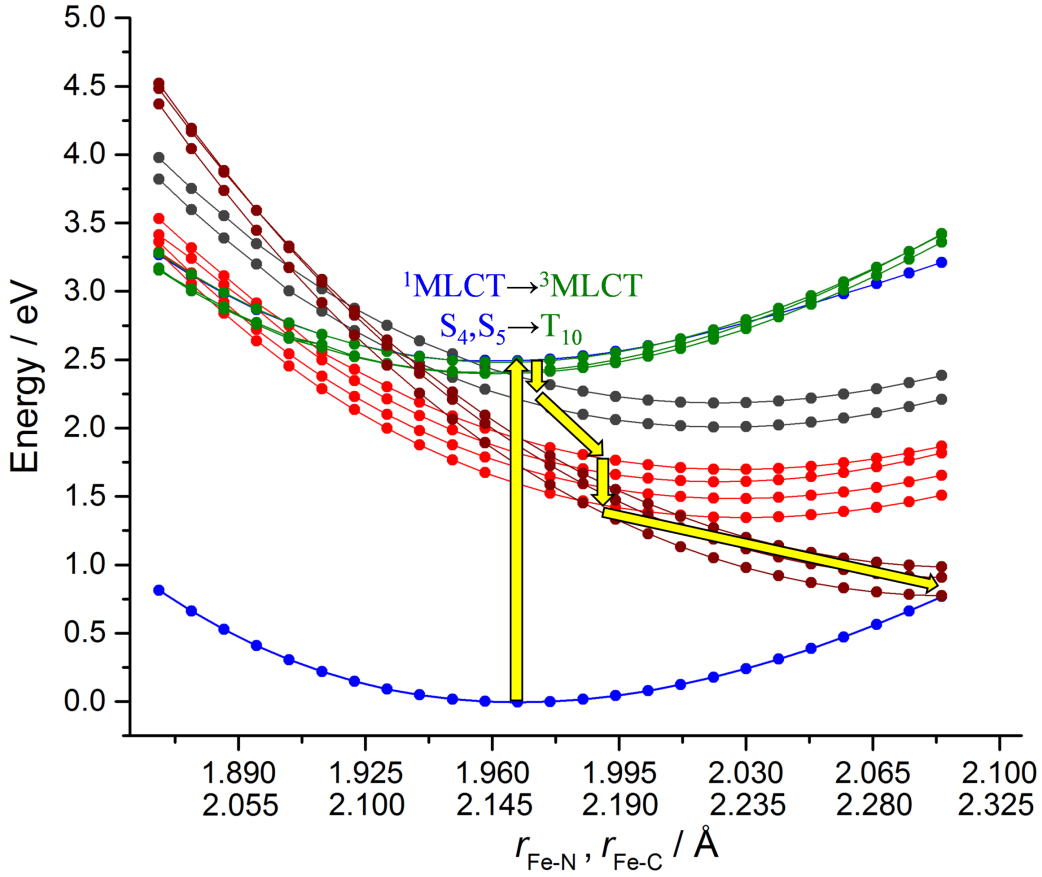

Figure 2: DFT/TD-DFT ground (^{1}GS) and excited state potential energy curves of $[Fe(btbip)_2]^{2+}$ along the breathing mode ν_4. Note that although all points represent geometries obtained by collective displacements along the normal mode, only the most relevant coordinates are indicated in the x axis of the figure: the Fe-N and Fe-C bond lengths. The color code illustrates the character of electronic states: ^{1}GS,^{1}MLCT – blue, ^{3}MLCT – green, ^{1}MC – dark grey, ^{3}MC – red, ^{5}MC – wine. Important transitions between electronic states expected from the energetics are schematically represented with yellow arrows.

Although the above analysis based on TD-DFT potentials delivers an qualitative insight into the potential photophysical decay pathways, it clearly suffers from the fact that it addresses dynamic transformations within a static representation. Moreover, all transition probabilities are obtained by considering only the energetics of potential energy curves along a single vibrational mode, i.e., neglecting the actual magnitude of couplings between various electronic states. In order to overcome these drawbacks, we performed spin-vibronic wavepacket quantum dynamics simulations which provide a detailed mechanistic understanding of the photodynamics of $[Fe(btbip)_2]^{2+}$.

Spin-Vibronic Hamiltonian

To investigate the excited state dynamics of $[Fe(btbip)_2]^{2+}$, we constructed a spin-vibronic model Hamiltonian,[22,24,25,48] which, as described previously, includes 4 nuclear DOF and 6 singlet/30 triplet, in overall 36 electronic states. Note that the TD-DFT potential energy curves along the four applied modes (Figures 2 and S10–S12) suggest that quintet states (^{5}MC) do not directly contribute to the decay of the MLCT states. This is confirmed by the negligible population of the ^{5}MC when performing a simulation using the quintet potentials instead those of the ^{3}MC states as shown in Figure S9. Furthermore, the practically vanishing (6 cm^{-1}) CASPT2 SOC between the ^{3}MLCT and ^{5}MC states of the related $[Fe(bipy)_3]^{2+}$ complex[5] also suggests the low possibility of a ^{3}MLCT$\rightarrow{}^5$MC relaxation channel. This is due to the fact that the orbital occupations between the two states differ by a double excitation and thus no direct SOC interaction can arise. Consequently, in subsequent simulations and discussion, we did not include quintet states and focus purely upon the dynamics between singlet and triplet excited states.

Figure 3 shows the TD-DFT potential energy curves, i.e., excitation energies along the most important normal modes, as well as their harmonic fit, from which the parameters of the diabatic vibronic coupling Hamiltonian were determined. The four applied vibrational modes are the following: ν_4 (83 cm^{-1}, a_1 (D_{2d}) symmetry), ν_{11} (112 cm^{-1}, b_2 symmetry),

ν_{16} (132 cm^{-1}, a_1 symmetry), and ν_{33} (295 cm^{-1}, a_1 symmetry) (for the animation of these modes, see the supplementary MPG files). Figure 3 shows that these normal modes of Fe-N/Fe-C stretching character are those which either drive nuclear motion (tuning modes: ν_4, ν_{16}, and ν_{33}) or induce various vibronic couplings (coupling mode: ν_{11}) most relevant to the photodynamics. This can be clearly seen in the horizontal displacement of MC potentials from the FC region in Figures 3a,c,d as well as in the splitting of those states which are degenerate at the FC point in Figure 3b. The inclusion of TD-DFT SOC matrix elements to the VCHAM yields the spin-vibronic Hamiltonian, which was used in the wavepacket quantum dynamics simulations of $[Fe(btbip)_2]^{2+}$ described below.

The Photorelaxation Mechanism

Figure 4a presents the population dynamics projected into the diabatic electronic states of ^{1}MLCT, ^{3}MLCT, ^{1}MC, and ^{3}MC character obtained by the propagation of the nuclear wavepacket from the initially excited ^{1}MLCT state. The first mechanistic step clearly corresponds to dynamics within the MLCT manifold. This involves two processes: i) ^{1}MLCT$\leftrightarrow^3$MLCT ISC proceeded by ii) the decay of MLCT states into MC states, both occuring on the ultrafast time scale. Exponential fits of the ^{1}MLCT and ^{3}MLCT populations yield lifetimes of 225 and 548 fs, respectively, which are in good agreement with the experimental $<$100 and 300 fs values. However, it is important to point out that these components are in fact not resolved in the transient absorption experiment,[13] only the combined process, i.e., the decay of the ^{1,3}MLCT, characterized by the 300 fs kinetic trace. This can be attributed to the very small energy gap and strong coupling between the S_4,S_5 ^{1}MLCT and T_{10} ^{3}MLCT states implying a high probability of both being initially excited by the pump pulse. A rather prominent result of this effect is the appearance of strong oscillations with a period of 100 fs in the population dynamics of singlet and triplet MLCT states, as can be seen in Figure 4a. These oscillations are induced by the constant perturbation in the electronic DOF, often referred to as Rabi oscillations in the case of a two-level system.

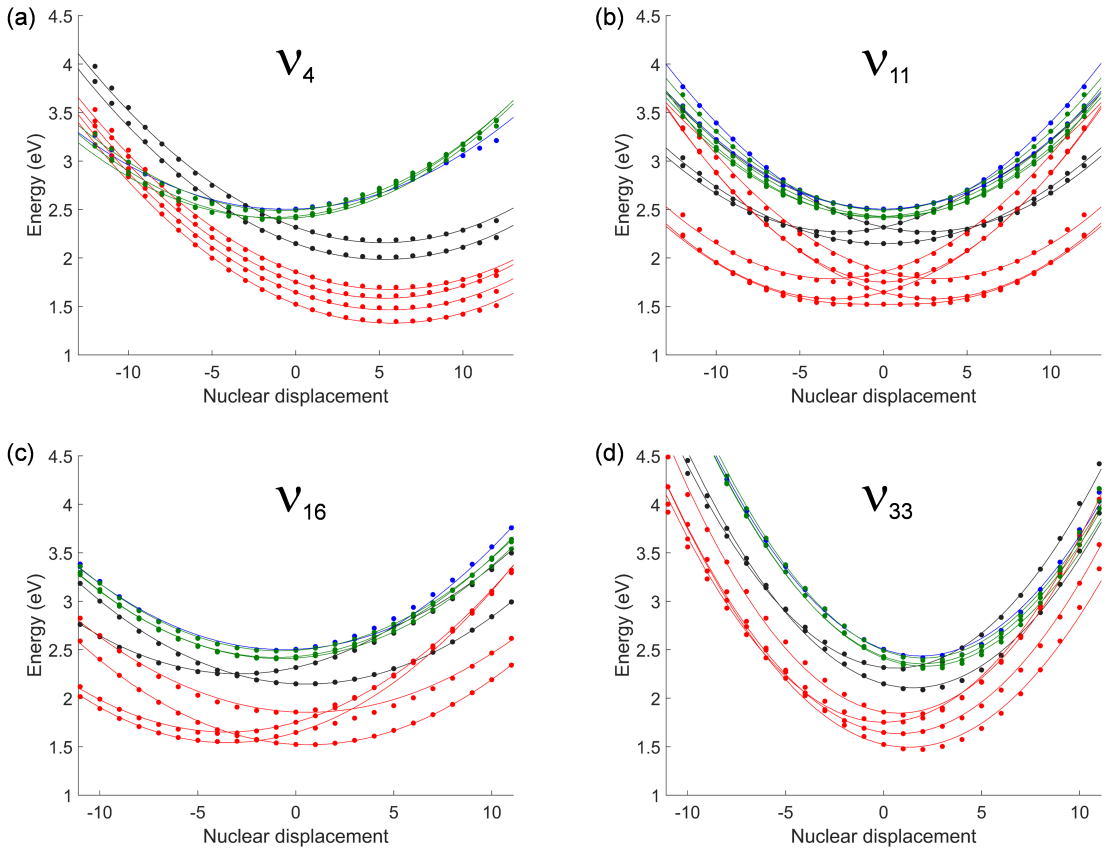

Figure 3: 1D cuts through the TD-DFT potentials of $[Fe(btbip)_2]^{2+}$ along the (a) ν_4, (c) ν_{16}, (d) ν_{33} tuning modes and the (b) ν_{11} coupling mode. The points represent TD-DFT energies along the 4 modes (nuclear displacements are shown in dimensionless mass-frequency weighted normal coordinates), while the lines correspond to their fit producing the diabatic VCHAM. The color code illustrates the character of electronic states: ^{1}MLCT – blue, ^{3}MLCT – green, ^{1}MC – dark grey, ^{3}MC – red.

In fact, the 100 fs period is in good agreement with the ∼170 fs value obtained from the Rabi frequency (Ω_R) as $1/\Omega_R = h/\sqrt{\Delta_{12}^2 + 4V_{12}^2}$,[49,50] where h is the Planck constant and Δ_{12}, V_{12} correspond to the 10 meV ^{1}MLCT-^{3}MLCT energy gap and the ∼11 meV absolute value of SOC, respectively. Therefore, the involved ^{1}MLCT and ^{3}MLCT states can be more properly described with the ^{1,3}MLCT term. By summing up the relative populations of the singlet and triplet MLCT components, the inverse phase coherences are destroyed, and the exponential fit of the ^{1,3}MLCT population shown in Figure 4b yields a lifetime of 350 fs in excellent agreement with the experimental 300 fs value.

The second mechanistic process reflects the formation and decay of ^{1}MC states, the latter characterized by a 497 fs time constant, obtained by the exponential fit to its population tail (Figure 4a). This relaxation step can occur with two mechanisms: either via nonadiabatic coupling from the ^{1}MLCT (internal conversion) or with SOC from the ^{3}MLCT state (ISC). In the present case, both channels are operative, as the values of corresponding couplings are comparable (Tables S4 and S6). The fact that these ^{1}MCs are the primary products of the MLCT decay indicates, as proposed previously from the quantum chemical calculations, that the ^{1}MC states are essential for the ultrafast decay of the ^{1,3}MLCT state. This is highlighted by performing the dynamics with the exclusion of ^{1}MCs, which results in the complete lack of the population of ^{3}MC states, i.e., the system is trapped in the ^{1,3}MLCT and only oscillates back and forth between the ^{1}MLCT and ^{3}MLCT components (Figure S8). Therefore, we report the key involvement of ^{1}MC states in the photorelaxation cascade as intermediates between ^{1,3}MLCT and ^{3}MC states. Although ^{1}MC states were included in the original ISC model as intitially excited states of Fe(II) complexes obtained by the pioneering work of A. Hauser *et al.*,[3] they have been generally ignored in the past two decades.

Further insight of the photorelaxation mechanism can be obtained by the analysis of the temporal evolution of nuclear wavepacket densities. In Figure 5, we show snapshots of the diabatic densities in the ^{3}MLCT and ^{1}MC states along modes ν_4 and ν_{11}. These results indicate that the wavepacket in the ^{3}MLCT state during the dynamics remains centered at a

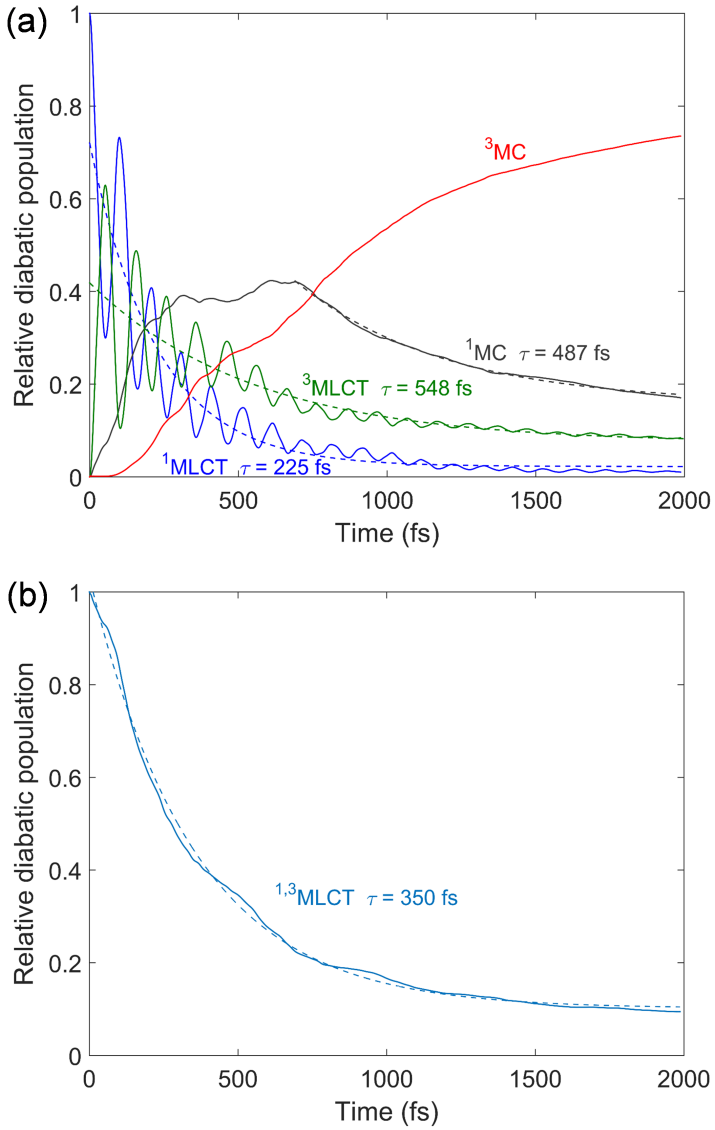

Figure 4: Relative diabatic populations of the (a) ^{1}MLCT, ^{3}MLCT, ^{1}MC, ^{3}MC, and (b) ^{1,3}MLCT (i.e., the sum of ^{1}MLCT and ^{3}MLCT populations) electronic states obtained from the quantum dynamics simulations initialized from the photoexcited ^{1}MLCT state. The dashed lines represent exponential fits to the corresponding population kinetics.

region of the excited state potential, which is very close to the FC point and the intersection of potential energy curves along mode ν_4. This and the ^{1}MC wavepacket densities imply that the ^{1,3}MLCT $\rightarrow$ ^{1}MC population transfer takes place at the above discussed area of the excited state potential, i.e., near the minimum energy geometry of MLCT states. The small MLCT-^{1}MC energy gap at this region leads to a very efficient transition between these states, which is the key to the ultrafast deactivation of the ^{1,3}MLCT states caused by *t*-Bu functionalization. Finally, it is important to point out that while breathing mode ν_4 plays a decisive role in the MLCT photodynamics, the antisymmetric stretching mode ν_{11} is crucial for the population transfer from the ^{1}MC to ^{3}MC states. This latter statement can be interpreted by the analysis of singlet and triplet MC potential energy curves, which show intersections along mode ν_{11} but not along mode ν_4 (Figures 3a and 3b).

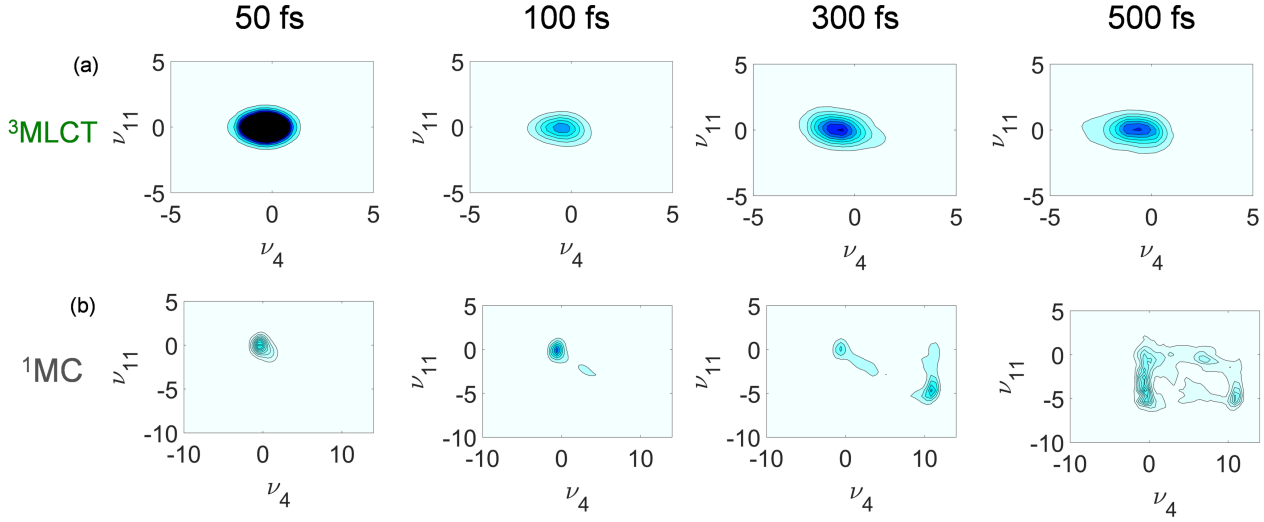

Figure 5: Snapshots of the nuclear wavepacket density along modes ν_4 and ν_{11} projected into the (a) ^{3}MLCT and (b) ^{1}MC diabatic electronic states at 50 fs, 100 fs, 300 fs, and 500 fs time delays after photoexcitation to the ^{1}MLCT state.

Conclusion

In the present work, we have presented a quantum chemistry and dynamics study to resolve the mechanism of the light-induced MLCT dynamics of $[Fe(btbip)_2]^{2+}$. The analysis of the energetics of potential energy curves along the lowest frequency breathing mode (ν_4) resulted in a valuable qualitative mechanistic picture of the photorelaxation. This comprises of an ultrafast ^{1}MLCT-^{3}MLCT ISC and conversion into the ^{1}MCs, followed by the population of ^{3}MC, and finally ^{5}MC states. With the quantum dynamics simulations, we revealed the details of the relaxation mechanism. Importantly, we found strong coupling between the ^{1}MLCT and ^{3}MLCT states, resulting in the ^{1,3}MLCT, whose simulated 350 fs excited state lifetime is in excellent agreement with the experimental value of 300 fs. We have identified ^{1}MCs as intermediates between MLCT and ^{3}MC states. Crucially, the ^{1,3}MLCT $\rightarrow$ ^{1}MC population transfer occurs at a region of the excited state potential, where the energy gap is small making the conversion very efficient.

Supporting Information Available

The following files are available free of charge.

- supportinginfo.pdf: parameters of the applied spin-vibronic Hamiltonian and supplementary results.
- vib4.mpg: animation of normal mode ν_4.
- vib11.mpg: animation of normal mode ν_{11}.
- vib16.mpg: animation of normal mode ν_{16}.
- vib33.mpg: animation of normal mode ν_{33}.

This material is available free of charge via the Internet at `http://pubs.acs.org/`.

Acknowledgement

The research leading to the presented results has received funding from the People Programme (Marie Curie Actions) of the European Union's Seventh Framework Programme (FP7/2007-2013) under REA grant agreement n^{o} 609405 (COFUNDPostdocDTU). The authors are grateful to Tobias Harlang and György Vankó for fruitful discussions.

References

(1) Gütlich, P.; Goodwin, H. A. *Spin Crossover in Transition Metal Compounds I*; Springer Berlin Heidelberg: Berlin, Heidelberg, 2004; Chapter Spin Crossover—An Overall Perspective, pp 1–47.

(2) Decurtins, S.; Gütlich, P.; Köhler, C.; Spiering, H.; Hauser, A. Light-Induced Excited Spin State Trapping in a Transition-Metal Complex: The Hexa-1-propyltetrazole-iron (II) Tetrafluoroborate Spin-Crossover System. *Chem. Phys. Lett.* **1984**, *105*, 1 – 4.

(3) Hauser, A.; Vef, A.; Adler, P. Intersystem Crossing Dynamics in Fe(II) Coordination Compounds. *J. Chem. Phys.* **1991**, *95*, 8710–8717.

(4) Cannizzo, A.; Milne, C.; Consani, C.; Gawelda, W.; Bressler, C.; van Mourik, F.; Chergui, M. Light-Induced Spin Crossover in Fe(II)-based Complexes: The Full Photocycle Unraveled by Ultrafast Optical and X-ray Spectroscopies. *Coord. Chem. Rev,* **2010**, *254*, 2677 – 2686.

(5) Sousa, C.; de Graaf, C.; Rudavskyi, A.; Broer, R.; Tatchen, J.; Etinski, M.; Marian, C. M. Ultrafast Deactivation Mechanism of the Excited Singlet in the Light-Induced Spin Crossover of $[Fe(2,2'\text{-bipyridine})_3]^{2+}$. *Chem. Eur. J.* **2013**, *19*, 17541–17551.

(6) Zhang, W.; Alonso-Mori, R.; Bergmann, U.; Bressler, C.; Chollet, M.; Galler, A.;

Gawelda, W.; Hadt, R.; Hartsock, R.; Kroll, T. et al. Tracking Excited-State Charge and Spin Dynamics in Iron Coordination Complexes. *Nature* **2014**, *509*, 345–348.

(7) Auböck, G.; Chergui, M. Sub-50-fs Photoinduced Spin Crossover in $[Fe(bpy)_3]^{2+}$. *Nat. Chem.* **2015**, *7*, 629–633.

(8) Kahn, O.; Martinez, C. J. Spin-Transition Polymers: From Molecular Materials Toward Memory Devices. *Science* **1998**, *279*, 44–48.

(9) Létard, J.-F.; Guionneau, P.; Goux-Capes, L. *Spin Crossover in Transition Metal Compounds III*; Springer Berlin Heidelberg: Berlin, Heidelberg, 2004; Chapter Towards Spin Crossover Applications, pp 221–249.

(10) Bousseksou, A.; Molnár, G.; Salmon, L.; Nicolazzi, W. Molecular Spin Crossover Phenomenon: Recent Achievements and Prospects. *Chem. Soc. Rev.* **2011**, *40*, 3313–3335.

(11) Monat, J. E.; ; McCusker, J. K. Femtosecond Excited-State Dynamics of an Iron(II) Polypyridyl Solar Cell Sensitizer Model. *J. Am. Chem. Soc.* **2000**, *122*, 4092–4097.

(12) Ardo, S.; Meyer, G. J. Photodriven Heterogeneous Charge Transfer with Transition-Metal Compounds Anchored to TiO_2 Semiconductor Surfaces. *Chem. Soc. Rev.* **2009**, *38*, 115–164.

(13) Liu, Y.; Harlang, T.; Canton, S. E.; Chábera, P.; Suárez-Alcántara, K.; Fleckhaus, A.; Vithanage, D. A.; Göransson, E.; Corani, A.; Lomoth, R. et al. Towards Longer-Lived Metal-to-Ligand Charge Transfer States of Iron(II) Complexes: An *N*-Heterocyclic Carbene Approach. *Chem. Commun.* **2013**, *49*, 6412–6414.

(14) Liu, Y.; Kjær, K. S.; Fredin, L. A.; Chábera, P.; Harlang, T.; Canton, S. E.; Lidin, S.; Zhang, J.; Lomoth, R.; Bergquist, K.-E. et al. A Heteroleptic Ferrous Complex with Mesoionic Bis(1,2,3-triazol-5-ylidene) Ligands: Taming the MLCT Excited State of Iron(II). *Chem. Eur. J.* **2015**, *21*, 3628–3639.

(15) Harlang, T.; Liu, Y.; Gordivska, O.; Fredin, L.; Ponseca, C.; Huang, P.; Chábera, P.; Kjaer, K.; Mateos, H.; Uhlig, J. et al. Iron Sensitizer Converts Light to Electrons with 92% Yield. *Nat. Chem.* **2015**, *7*, 883–889.

(16) Grätzel, M. Dye-Sensitized Solar Cells. *J. Photochem. Photobiol. C* **2003**, *4*, 145 – 153.

(17) Meyer, T. J. Chemical Approaches to Artificial Photosynthesis. *Acc. Chem. Res.* **1989**, *22*, 163–170.

(18) Alstrum-Acevedo, J. H.; Brennaman, M. K.; Meyer, T. J. Chemical Approaches to Artificial Photosynthesis. 2. *Inorg. Chem.* **2005**, *44*, 6802–6827.

(19) Kumar, B.; Llorente, M.; Froehlich, J.; Dang, T.; Sathrum, A.; Kubiak, C. P. Photochemical and Photoelectrochemical Reduction of CO_2. *Annu. Rev. Phys. Chem.* **2012**, *63*, 541–569.

(20) Fredin, L. A.; Pápai, M.; Rozsályi, E.; Vankó, G.; Wärnmark, K.; Sundström, V.; Persson, P. Exceptional Excited-State Lifetime of an Iron(II)-*N*-Heterocyclic Carbene Complex Explained. *J. Phys. Chem. Lett.* **2014**, *5*, 2066–2071.

(21) Pápai, M.; Vankó, G.; Rozgonyi, T.; Penfold, T. J. High-Efficiency Iron Photosensitizer Explained with Quantum Wavepacket Dynamics. *J. Phys. Chem. Lett.* **2016**, *7*, 2009–2014.

(22) Capano, G.; Chergui, M.; Rothlisberger, U.; Tavernelli, I.; Penfold, T. J. A Quantum Dynamics Study of the Ultrafast Relaxation in a Prototypical Cu(I)–Phenanthroline. *J. Phys. Chem. A* **2014**, *118*, 9861–9869.

(23) Gourlaouen, C.; Eng, J.; Otsuka, M.; Gindensperger, E.; Daniel, C. Quantum Chemical Interpretation of Ultrafast Luminescence Decay and Intersystem Crossings in Rhenium(I) Carbonyl Bipyridine Complexes. *J. Chem. Theory Comput.* **2015**, *11*, 99–110.

(24) Eng, J.; Gourlaouen, C.; Gindensperger, E.; Daniel, C. Spin-Vibronic Quantum Dynamics for Ultrafast Excited-State Processes. *Acc. Chem. Res.* **2015**, *48*, 809–817.

(25) Harabuchi, Y.; Eng, J.; Gindensperger, E.; Taketsugu, T.; Maeda, S.; Daniel, C. Exploring the Mechanism of Ultrafast Intersystem Crossing in Rhenium(I) Carbonyl Bipyridine Halide Complexes: Key Vibrational Modes and Spin-Vibronic Quantum Dynamics. *J. Chem. Theory Comput.* **2016**, *12*, 2335–2345.

(26) Cederbaum, L. S.; Köppel, H.; Domcke, W. Multimode Vibronic Coupling Effects in Molecules. *Int. J. Quantum Chem.* **1981**, *20*, 251–267.

(27) Köppel, H.; Domcke, W.; Cederbaum, L. S. *Advances in Chemical Physics*; John Wiley & Sons, Inc., 2007; pp 59–246.

(28) Seidner, L.; Stock, G.; Sobolewski, A. L.; Domcke, W. *Ab Initio* Characterization of the S1-S2 Conical Intersection in Pyrazine and Calculation of Spectra. *J. Chem. Phys.* **1992**, *96*, 5298–5309.

(29) Markmann, A.; Worth, G. A.; Cederbaum, L. S. Allene and Pentatetraene Cations as Models for Intramolecular Charge Transfer: Vibronic Coupling Hamiltonian and Conical Intersections. *J. Chem. Phys.* **2005**, *122*.

(30) Worth, G. A.; Welch, G.; Paterson, M. J. Wavepacket Dynamics Study of $Cr(CO)_5$ After Formation by Photodissociation: Relaxation Through an $(E \oplus A) \otimes e$ Jahn-Teller Conical Intersection. *Mol. Phys.* **2006**, *104*, 1095–1105.

(31) Penfold, T. J.; Worth, G. A. A Model Hamiltonian to Simulate the Complex Photochemistry of Benzene II. *J. Chem. Phys.* **2009**, *131*.

(32) Assmann, M.; Worth, G. A.; González, L. 9D Nonadiabatic Quantum Dynamics Through a Four-State Conical Intersection: Investigating the Homolysis of the O-O Bond in Anthracene-9,10-endoperoxide. *J. Chem. Phys.* **2012**, *137*.

(33) Kuhlman, T. S.; Sauer, S. P. A.; Sølling, T. I.; Møller, K. B. Symmetry, Vibrational Energy Redistribution and Vibronic Coupling: The Internal Conversion Processes of Cycloketones. *J. Chem. Phys.* **2012**, *137*.

(34) Reiher, M.; Salomon, O.; Artur Hess, B. Reparameterization of Hybrid Functionals Based on Energy Differences of States of Different Multiplicity. *Theor. Chem. Acc.* **2001**, *107*, 48–55.

(35) Hirata, S.; Head-Gordon, M. Time-Dependent Density Functional Theory within the Tamm-Dancoff Approximation. *Chem. Phys. Lett.* **1999**, *314*, 291 – 299.

(36) Neese, F. The ORCA Program System. *WIREs Comput. Mol. Sci.* **2012**, *2*, 73–78.

(37) Pápai, M.; Vankó, G.; de Graaf, C.; Rozgonyi, T. Theoretical Investigation of the Electronic Structure of Fe(II) Complexes at Spin-State Transitions. *J. Chem. Theory Comput.* **2013**, *9*, 509–519.

(38) Vankó, G.; Bordage, A.; Pápai, M.; Haldrup, K.; Glatzel, P.; March, A. M.; Doumy, G.; Britz, A.; Galler, A.; Assefa, T. et al. Detailed Characterization of a Nanosecond-Lived Excited State: X-ray and Theoretical Investigation of the Quintet State in Photoexcited $[Fe(terpy)_2]^{2+}$. *J. Phys. Chem. C* **2015**, *119*, 5888–5902.

(39) Ordejón, B.; de Graaf, C.; Sousa, C. Light-Induced Excited-State Spin Trapping in Tetrazole-Based Spin Crossover Systems. *J. Am. Chem. Soc.* **2008**, *130*, 13961–13968.

(40) Levine, B. G.; Ko, C.; Quenneville, J.; Martínez, T. J. Conical Intersections and Double Excitations in Time-Dependent Density Functional Theory. *Mol. Phys.* **2006**, *104*, 1039–1051.

(41) Martin, R. L. Natural Transition Orbitals. *J. Chem. Phys.* **2003**, *118*, 4775–4777.

(42) van Lenthe, E.; Baerends, E. J.; Snijders, J. G. Relativistic Regular Two-Component Hamiltonians. *J. Chem. Phys.* **1993**, *99*, 4597–4610.

(43) van Lenthe, E.; Baerends, E. J.; Snijders, J. G. Relativistic Total Energy Using Regular Approximations. *J. Chem. Phys.* **1994**, *101*, 9783–9792.

(44) Wang, F.; Ziegler, T. A Simplified Relativistic Time-Dependent Density-Functional Theory Formalism for the Calculations of Excitation Energies Including Spin-Orbit Coupling Effect. *J. Chem. Phys.* **2005**, *123*, 154102.

(45) te Velde, G.; Bickelhaupt, F. M.; Baerends, E. J.; Fonseca Guerra, C.; van Gisbergen, S. J. A.; Snijders, J. G.; Ziegler, T. Chemistry with ADF. *J. Comput. Chem.* **2001**, *22*, 931–967.

(46) Meyer, H.-D.; Manthe, U.; Cederbaum, L. The Multi-Configurational Time-Dependent Hartree Approach. *Chem. Phys. Lett.* **1990**, *165*, 73 – 78.

(47) Beck, M.; Jäckle, A.; Worth, G.; Meyer, H.-D. The Multiconfiguration Time-Dependent Hartree (MCTDH) Method: A Highly Efficient Algorithm for Propagating Wavepackets. *Phys. Rep.* **2000**, *324*, 1 – 105.

(48) Capano, G.; Penfold, T. J.; Röthlisberger, U.; Tavernelli, I. A Vibronic Coupling Hamiltonian to Describe the Ultrafast Excited State Dynamics of a Cu(I)-Phenanthroline Complex. *Chimia* **2014**, *68*, 227–230.

(49) Grossmann, F. *Theoretical Femtosecond Physics – Atoms and Molceules in Strong Laser Fields*; Springer International Publishing, 2008.

(50) Chang, J.; Fedro, A. J.; van Veenendaal, M. Ultrafast Electron Dynamics Theory of Photo-Excited Ruthenium Complexes. arXiv:1003.4752, 2010.

For Table of Contents Only